Magnonic Weyl states in Cu₂OSeO₃

L.-C. Zhang, ^{1,2} Y. A. Onykiienko, ³ P. M. Buhl, ⁴ Y. V. Tymoshenko, ³ P. Čermák, ^{5,6} A. Schneidewind, ⁵ J. R. Stewart, ⁷ A. Henschel, ⁸ M. Schmidt, ⁸ S. Blügel, ¹ D. S. Inosov, ^{3,*} and Y. Mokrousov^{1,4,*}

¹Peter Grünberg Institut and Institute for Advanced Simulation, Forschungszentrum Jülich and JARA, 52425 Jülich, Germany ²Department of Physics, RWTH Aachen University, 52056 Aachen, Germany

³Institut für Festkörper- und Materialphysik, Technische Universität Dresden, 01069 Dresden, Germany
⁴Institute of Physics, Johannes Gutenberg University Mainz, 55099 Mainz, Germany

⁵Forschungszentrum Jülich GmbH, Jülich Center for Neutron Science at MLZ, Lichtenbergstraße 1, 85748 Garching, Germany ⁶Charles University, Faculty of Mathematics and Physics, Department of Condensed Matter Physics, Ke Karlovu 5, 121 16 Praha, Czech Republic

⁷ISIS Neutron and Muon Source, STFC Rutherford Appleton Laboratory, Harwell Campus, Didcot OX11 0QX, United Kingdom
⁸Max Planck Institute for Chemical Physics of Solids, Nöthnitzer Straße 40, 01187 Dresden, Germany



(Received 18 January 2019; published 21 January 2020)

The multiferroic ferrimagnet Cu_2OSeO_3 with a chiral crystal structure has attracted a lot of recent attention due to the emergence of a magnetic skyrmion order in this material. Here, the topological properties of its magnon excitations are systematically investigated by linear spin-wave theory and inelastic neutron scattering. When considering Heisenberg exchange interactions only, two degenerate Weyl magnon nodes with topological charges ± 2 are observed at high-symmetry points. Each Weyl point splits into two as the symmetry of the system is further reduced by including into consideration the nearest-neighbor Dzyaloshinskii-Moriya interaction, crucial for obtaining an accurate fit to the experimental spin-wave spectrum. Also, one additional pair of Weyl points appears near the $\bf R$ point. The predicted topological properties are verified by surface state and Chern number analysis. Additionally, we predict that a measurable thermal Hall conductivity can be associated with the emergence of the Weyl points, the position and number of which can be tuned by modifying the Dzyaloshinskii-Moriya interaction in the system.

DOI: 10.1103/PhysRevResearch.2.013063

I. INTRODUCTION

Topological insulators and Weyl semimetals have attracted tremendous attention as the most prominent realizations of topologically nontrivial electronic matter [1–5]. In recent years, topologically protected band touching points, known as Weyl nodes, were observed in electronic [6–8], photonic [9], phononic [10], and magnetic excitation spectra [11–13]. In relationship to magnetically ordered materials, new concepts of topological magnon insulators [14–17], topological spinon semimetals [18], and Dirac and Weyl magnon states [19–26] were introduced, offering promising new applications in the emerging field of spintronics [27–30].

Experimentally, topologically nontrivial magnon states were recently identified in a two-dimensional spin- $\frac{1}{2}$ kagomelattice ferromagnet [11] and in the three-dimensional (3D) antiferromagnet Cu_3TeO_6 by two independent groups [12,13]

Published by the American Physical Society under the terms of the Creative Commons Attribution 4.0 International license. Further distribution of this work must maintain attribution to the author(s) and the published article's title, journal citation, and DOI.

using inelastic neutron scattering (INS). On the theory side, it has been realized that chiral magnets offer a generic route to the realization of topological magnon states, representing a magnon analog of topological insulators. As a result of an antisymmetric exchange, known as the Dzyaloshinskii-Moriya interaction (DMI) [31,32], the bulk magnon spectrum of a chiral magnet can acquire a topological energy gap that supports a topologically protected gapless Dirac cone in the surface magnon spectrum [17]. A similar mechanism based on DMI was also proposed for the formation of magnonic Weyl crossing points in the spin-wave spectrum of the noncoplanar antiferromagnetic (AFM) state on a breathing-pyrochlore lattice [19,20,25].

The cubic copper(II)-oxoselenite Cu_2OSeO_3 is a multiferroic ferrimagnet with a chiral crystal structure that came under the focus of recent attention owing to the emergence of skyrmion order in this material [33–37]. Its crystal structure is cubic (space group $P2_13$) with a lattice constant a=8.925 Å [38]. The magnetic sublattice of Cu^{2+} ions can be approximated as a distorted breathing-pyrochlore lattice, consisting of slightly deformed tetrahedral Cu_4 clusters in a face-centered-cubic (fcc) arrangement [39]. Magnetic interactions within the tetrahedron lead to a ferrimagnetic ground state, in which one of the Cu^{2+} spins is antiparallel to the other three, resulting in a total spin S=1 of the cluster [40–42]. Weaker interactions between the clusters lead to a long-range spin-spiral order that

^{*}Corresponding authors: dmytro.inosov@tu-dresden.de; y.mokrousov@fz-juelich.de

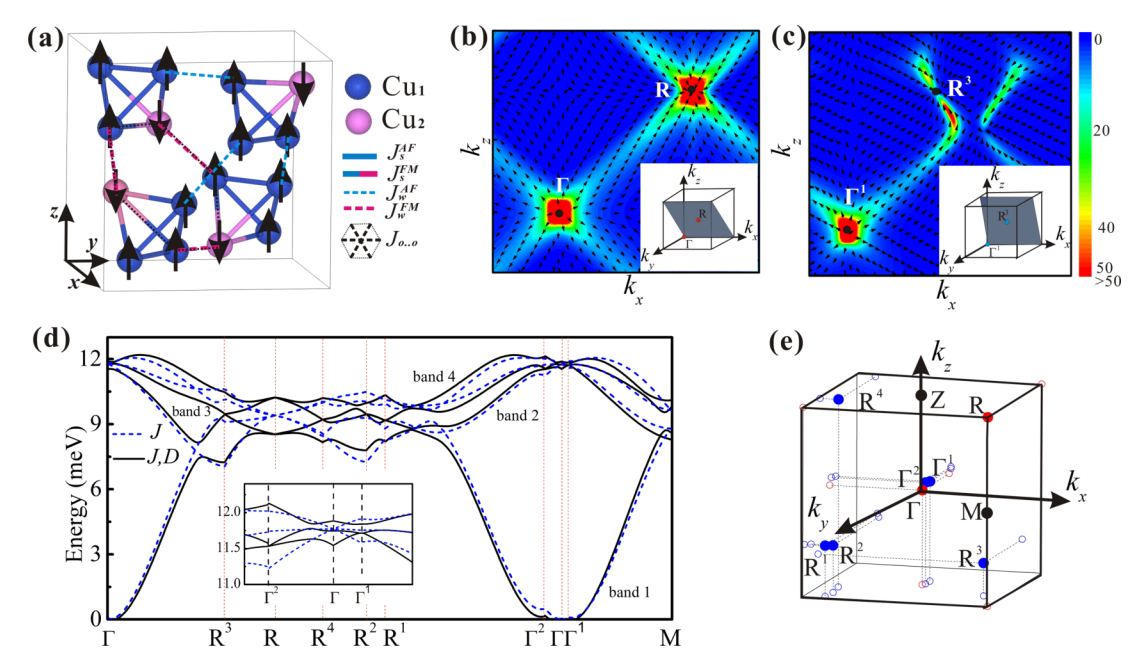


FIG. 1. (a) The structure of ferrimagnetic Cu_2OSeO_3 is shown together with five different interaction paths, marked by J_s^{FM} , J_s^{AFM} , J_w^{AFM} , and $J_{0..0}$, where $J_{0..0}$ represents the antiferromagnetic long-range interaction. (b), (c) Monopole distribution of the absolute magnitude of the Berry curvature corresponding to the two lowest magnon bands in the k planes marked in the inset. In (b), the DMI was not taken into account, while (c) shows the result with the DMI included. The k planes are chosen so that they include the Weyl points. (d) The magnon dispersion of the lowest four bands of Cu_2OSeO_3 . The dotted blue line represents the dispersion without the effect of the DMI, with the Weyl points emerging at \mathbf{R} and at $\mathbf{\Gamma}$. The black line represents the dispersion upon including the DMI, with six Weyl points emerging at \mathbf{R}^1 , \mathbf{R}^2 , \mathbf{R}^3 , \mathbf{R}^4 , $\mathbf{\Gamma}^1$, and $\mathbf{\Gamma}^2$. The exact positions of the Weyl points are shown in (e): $\mathbf{R}^1 = (-0.39, 0.47, -0.23)$, $\mathbf{R}^2 = (-0.38, 0.34, -0.25)$, $\mathbf{R}^3 = (0.40, 0.22, -0.33)$, $\mathbf{R}^4 = (-0.40, 0.18, 0.49)$, $\mathbf{\Gamma}^1 = (0.01, -0.03, 0.04)$, $\mathbf{\Gamma}^2 = (0.01, -0.11, 0.03)$, and their unit-direction projections are indicated by blue open circles.

sets in below $T_{\rm C}\approx 57$ K. The helical spin order is observed with a wave number $q\approx 0.01$ Å $^{-1}$ which corresponds to a modulation period of approximately 63 nm in the [001] direction [34]. Existing magnetic models [40–43] consider up to five Heisenberg exchange interactions and up to five DMI vectors. These models were used to describe the INS spectrum of spin-wave excitations in a broad energy range and in the whole reciprocal space [39], as well as electron spin resonance (ESR) that probes spin-wave excitations at the zone center [44]. However, the DMI was initially neglected in these studies.

This simplified description, that involves only Heisenberg interactions, provides a qualitatively good fit to the experimental spin-wave dispersion over the entire Brillouin zone [39] with the exception of the zone corner (\mathbf{R} point), where the magnon bands remain degenerate for any values of the exchange parameters. Tucker *et al.* [45] recently showed that this degeneracy is removed by DMI, leading to a clearly resolved spin gap of ~ 1.6 meV in the magnon spectrum, which they observed by neutron spectroscopy. These observations are a strong indication for the existence of topological magnon states in Cu_2OSeO_3 , which motivated our present study.

In the following, we present spin-dynamical calculations of the magnon spectrum in the presence of DMI that was adjusted to provide the best fit to the experimental spin-wave dispersion in the vicinity of the **R** point. Using linear spin-wave theory (LSWT) in combination with high-resolution neutron spectroscopy, we show that, in the absence of DMI terms, two pairs of degenerate Weyl nodes with the

topological charge +2 and -2 are located at the zone center (Γ point) and at the zone boundary (\mathbf{R} point). Consideration of the nearest-neighbor DMI is sufficient to lift the degeneracy of these Weyl nodes, so that they are shifted away from the high-symmetry points into a position that sensitively depends on the direction and magnitude of the DMI vector. Other than this, one pair of Weyl points is predicted to appear near the R points. A direct observation of the resulting Weyl points would offer a possibility to accurately extract the DMI from INS measurements. We verify the predicted topological properties by a Chern number analysis and give quantitative predictions for the location of magnonic Weyl points in the spin-wave spectrum. We also analyze topologically protected magnon surface states and estimate the magnonic contribution to the thermal Hall conductivity that may serve as robust hallmarks of the emergent topological states in Cu₂OSeO₃, awaiting direct experimental verification.

II. RESULTS

A. Magnetic model, experimental result, and magnon spectrum

The crystal structure of Cu_2OSeO_3 belongs to the chiral space group $P2_13$ and contains 16 magnetic Cu^{2+} ions per unit cell with $S=\frac{1}{2}$. They occupy two structurally nonequivalent positions, so that every Cu_4 tetrahedral cluster consists of one Cu(1) ion on the 4a Wyckoff site and three Cu(2) ions on the 12b site [38,46] (see Fig. 1). The strong superexchange coupling $J_s^{\rm FM}$ between the Cu(2) ions within the cluster is ferromagnetic (FM), whereas the Cu(1) and Cu(2) spins

TABLE I. Values of the parameters entering the Heisenberg Hamiltonian (1). Five exchange interactions are listed together with the corresponding interatomic distances which are very similar to previous works. The nearest-neighbor DMI vector was chosen so as to reproduce the experimental spin-wave dispersion.

| Parameters | Distance (Å) | J (meV) [39] | D (meV) |
|----------------------|--------------|--------------|----------------------|
| $J_{ m w}^{ m FM}$ | 3.039 | -4.2 | (-0.491, 2.0, -1.41) |
| $J_{ m s}^{ m AFM}$ | 3.057 | 12.3 | 0 |
| $J_{ m s}^{ m FM}$ | 3.22 | -14.5 | 0 |
| $J_{ m w}^{ m AFM}$ | 3.30 | 2.33 | 0 |
| $J_{ m OO}^{ m AFM}$ | 6.35 | 3.88 | 0 |

within the same tetrahedron are coupled antiferromagnetically with a coupling constant $J_{\rm s}^{\rm AFM}$. These exchange constants constitute the dominant magnetic interactions that lead to a ferrimagnetic spin arrangement within the cluster: Three Cu(2) spins align ferromagnetically, and the Cu(1) spin is pointing in the opposite direction, resulting in a total spin of S=1 [47]. The intercluster interactions are considerably weaker, given by the FM superexchange $J_{\rm w}^{\rm FM}$ between the nearest Cu(2) ions of neighboring clusters, the weak AFM coupling $J_{\rm w}^{\rm AFM}$ between Cu(1) and Cu(2), and a longer-range exchange $J_{\rm O,O}^{\rm AFM}$ that connects Cu(1) and Cu(2) sites across the diagonals of alternating Cu(1)-Cu(2) hexagon loops [41] (see Fig. 1).

Numerical values of all five Heisenberg interactions have been calculated from the microscopic electronic structure theory and verified using thermodynamic data [42], terahertz ESR [44], far-infrared [43] and Raman [48] spectroscopy, and INS measurements [39,45] in earlier works. As a result, there are accurate quantitative estimates of all five exchange parameters. On the other hand, antisymmetric DMI is also allowed by crystal symmetry along all mentioned exchange paths. Each DMI channel can add at most three extra parameters, which are the off-diagonal components of the \hat{J} tensor. This results in up to 15 additional parameters in the magnetic Hamiltonian. All previously reported attempts to estimate their magnitude are based on first-principles calculations [42]. Hence, the measurable DMI signatures in the spin-wave spectrum [45] still await experimental verification.

Here, we use LSWT to calculate the magnon spectrum of Cu₂OSeO₃, starting from the generalized Heisenberg model,

$$H = \sum_{\langle i,i \rangle} \mathbf{S}_i^{\dagger} \hat{J}_{ij} \mathbf{S}_j, \tag{1}$$

where the interaction tensor between the lattice sites i and j,

$$\hat{J}_{ij} = \begin{pmatrix} J_{ij}^{x} & D_{ij}^{z} & -D_{ij}^{y} \\ -D_{ij}^{z} & J_{ij}^{y} & D_{ij}^{x} \\ D_{ij}^{y} & -D_{ij}^{x} & J_{ij}^{z} \end{pmatrix}, \tag{2}$$

includes the symmetric exchange \mathbf{J}_{ij} and the antisymmetric off-diagonal DMI terms \mathbf{D}_{ij} , caused by the spin-orbit coupling. The DMI vector is defined as $\mathbf{D}_{ij} = (D_{ij}^x, D_{ij}^y, D_{ij}^z)$. Following earlier works [39], we include five Heisenberg exchange interactions shown in Fig. 1(a), with their numerical values listed in Table I. To deal with the ferrimagnetic system,

the rotation matrix O_i is introduced, where O_i determines the magnetic moment direction at the site i.

To get the magnons excitation spectrum, the LSWT is used [21,49–51], where the Holstein-Primakoff transformation [52] is adopted for the quantum spin operators. A Fourier transformation of the boson operators is given by

$$\alpha_l(\mathbf{k}) = \begin{pmatrix} a_l(\mathbf{k}) \\ a_l^{\dagger}(-\mathbf{k}) \end{pmatrix} = \frac{1}{\sqrt{N}} \sum_m e^{-i\mathbf{k}\mathbf{R_m}} \begin{pmatrix} a_{lm} \\ a_{lm}^{\dagger} \end{pmatrix}, \quad (3)$$

where N is the number of the unit cells, and \mathbf{k} is the vector in the reciprocal k space of magnons (suppressed below for convenience). The Fourier-transformed Hamiltonian part quadratic in the boson operators, denoted as H_2 , becomes a $2n \times 2n$ matrix, where n is the number of atoms in the unit cell. From the commutation relation between the bosonic creation (annihilation) operators and H_2 , we arrive at the equation

$$i\frac{d\alpha_l}{dt} = [\alpha_l, H_2] = \sum_m D_{lm} \alpha_m, \tag{4}$$

where the dynamical matrix is given by $D = gH_2$ with g = [(1,0),(0,-1)], where 1 is the $n \times n$ identity matrix. The positive real eigenvalues of the dynamical matrix D correspond to the magnon excitation spectrum in the system. While the left and right eigenvectors of D, denoted as V^L and V^R , may differ since D is not necessarily Hermitian, their relation is trivially given by $V^L = gV^{R\dagger}g$.

The first INS experiment has been carried out using the cold-neutron triple-axis spectrometer PANDA [53] located at MLZ in Garching, Germany. The sample is a coaligned mosaic of 11 single crystals with a total mass of \sim 2 g and a mosaicity of \sim 2°. It was mounted in the (*HHL*) scattering plane, i.e., with the [110] axis vertical, inside the JVM1-5.0T cryomagnet with a base temperature of 1.5 K. The instrument was operated with a fixed final neutron wavelength $k_f = 1.5 \text{ Å}^{-1}$. To avoid higher-order contamination from the monochromator, a cold beryllium filter was mounted between the sample and the analyzer. The second follow-up experiment was carried out at the time-of-flight (TOF) spectrometer MAPS [54] at ISIS (Didcot, U.K.) with the incident neutron energy $E_i = 25 \text{ meV}$ to map out the whole energy-momentum space including low-symmetry directions [55].

The magnon spectrum of Cu₂OSeO₃ has been analyzed in several previous works, which used similar values of the exchange parameters J and neglected the effect of the DMI [39,41,45]. In these works, similar magnon dispersions were obtained, featuring two doubly degenerate crossing points: one at Γ and one at R high-symmetry points. The results of our calculations, performed without DMI, are very close to previously published data, and they are shown in Fig. 1(d). On the other hand, the results of our high-resolution INS measurements, presented in Fig. 2, clearly mark the formation of a 1.6-meV band gap at **R** between bands 2 and 3, according to the enumeration of Fig. 1(d). To reproduce this band gap in the calculations, we have chosen the value of the nearestneighbor DMI by fitting it to the experimental data in terms of the magnon spectrum and pitch of the spin-spiral ground state (see Fig. S5 of the Supplemental Material [56]). The values of fitted J and D parameters are listed in Table I, whereas

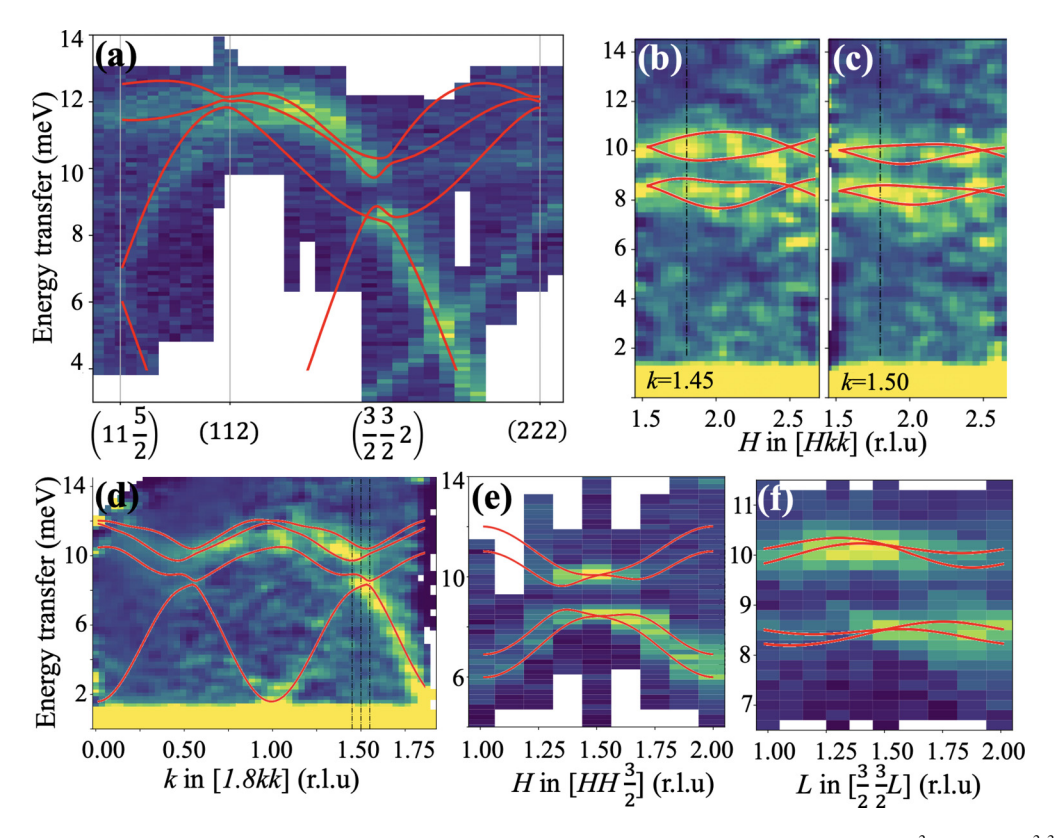


FIG. 2. Momentum-energy cuts along (a) (11L)-(HH2), (b) (1.45KK), (c) (1.5KK), (d) (1.8KK), (e) $(HH\frac{3}{2})$, and (f) $(\frac{3}{2}\frac{3}{2}L)$ directions in reciprocal space. All measurements were done at 2 K without applying magnetic field. Data in (a), (e), and (f) were measured at the triple-axis spectrometer, while (b)–(d) are cuts from the TOF data set, integrated within ± 0.1 r.l.u. in momentum directions orthogonal to the figure plane. The magnon dispersion calculated with the fitted value of the DMI is shown with thin red lines. The straight feature in the bottom-right-hand corner of (a), which is not captured by the spin-wave model, is a spurious peak from nonmagnetic multiple scattering. The magnon dispersion along the paths which do not contain high-symmetry points is shown in (b) and (d). The last two cuts (e) and (f) are centered at the $\mathbf{R}(\frac{3}{2},\frac{3}{2},\frac{3}{2})$ point, where degenerate magnon bands are predicted in the absence of DMI.

Fig. 2 shows a comparison of the experimental and calculated magnon spectra. The value of the DMI that we use in this work provided by far the best fit to the experiment among other possible DMI choices, which, e.g., included more neighbors into consideration, or even with respect to previously published *ab initio* results for the DMI in this system [42] (see Figs. S2 and S3 of the Supplemental Material [56]). The overall agreement between theoretical and experimental data presented in Fig. 2 is excellent.

Irrespective of its exact choice, including the DMI into the picture has a drastic effect on the number and position of the degenerate crossings between bands 2 and 3 in the magnonic band structure, while the position of these degenerate crossings at high-symmetry points without the DMI is enforced by the crystal symmetry. The set of DMI parameters we used here (see Table I), splits previously degenerate crossing points at Γ and **R**, giving rise to six crossings overall: two at \mathbb{R}^3 and \mathbb{R}^4 (in the vicinity of **R**), two at Γ^1 and Γ^2 (in the vicinity of Γ), and one additional pair of new crossing points at \mathbf{R}^1 and \mathbf{R}^2 [see Figs. 1(d) and 1(e)]. Given state-of-the-art experimental conditions, we were unable to obtain the neutron scattering evidence (e.g., in terms of a characteristic intensity pattern [57]) for the predicted crossing points, which can be partly attributed to their asymmetric positioning in the Brillouin zone and the respective necessity of scanning through the directions which contain them. However, given the excellent agreement between theory and experiment apparent in Fig. 2, we are confident that our theoretical model reproduces the magnonic spectrum of Cu₂OSeO₃ throughout the whole Brillouin zone well and that the degeneracy points predicted by the model can be eventually resolved experimentally in the future. In the next section we analyze the topological character of these points.

B. Topological properties

In order to access the topological properties of the system, we calculate the Berry curvature of each magnonic band n, defined as [20,51]

$$\mathbf{\Omega}_{n}(\mathbf{k}) = -\sum_{m \neq n} \frac{\operatorname{Im}\left[\left\langle V_{n\mathbf{k}}^{L} \middle| \partial_{\mathbf{k}} D(\mathbf{k}) \middle| V_{n\mathbf{k}}^{R} \right\rangle \times \left\langle V_{n\mathbf{k}}^{L} \middle| \partial_{\mathbf{k}} D(\mathbf{k}) \middle| V_{n\mathbf{k}}^{R} \right\rangle\right]}{(\epsilon_{n\mathbf{k}} - \epsilon_{m\mathbf{k}})^{2}},$$
(5)

where $\epsilon_{m\mathbf{k}}$ and $\epsilon_{n\mathbf{k}}$ are the magnonic eigenvalues.

As we mainly focus on the topological nature of the band crossings arising between bands 2 and 3, we analyze the cumulative Berry curvature of bands 1 and 2. In Fig. 1(b) we present the direction of the normalized projected cumulative Berry curvature vector field and its absolute magnitude in the $k_y = k_z$ plane, first for the case without DMI. In the mentioned figure, the color scale represents the absolute value of the Berry curvature vector field. As apparent from the figure, the Berry curvature distribution exhibits two monopolelike

features at \mathbf{R} and $\mathbf{\Gamma}$, where the band crossings occur, with the crossing at $\mathbf{\Gamma}$ serving as a source, and the crossing at \mathbf{R} serving as a sink of the Berry curvature field. The corresponding distribution, obtained after including the DMI, is shown in Fig. 1(c) in the plane which includes $\mathbf{\Gamma}^1$ and \mathbf{R}^3 points and which is perpendicular to the k_y - k_z plane. In the latter case the distribution of the Berry curvature field, although similar to the previous case, is more complex, owing to the fact that the crossings at $\mathbf{\Gamma}^2$, \mathbf{R}^1 , \mathbf{R}^2 , and \mathbf{R}^4 are very close to the plane so that the overall distribution coming from all six points is plotted.

Next, we compute the monopole charge of the ith band crossing by evaluating the flux of the cumulative Berry curvature field of the lowest two bands through an infinitesimal two-dimensional sphere S_i surrounding the crossing,

$$Q_i = \frac{1}{2\pi} \int_{S_i} \mathbf{\Omega}(\mathbf{k}) \cdot \mathbf{n} \, dS_i, \tag{6}$$

where $\bf n$ is the surface normal. According to our calculations, without the DMI, the total topological charge of the two degenerate points at $\bf \Gamma$ is +2, while it constitutes a value of -2 at $\bf R$. Upon including the effect of the DMI, each of the double degeneracies splits into two nondegenerate points with charges of +1 at $\bf \Gamma^1$ and $\bf \Gamma^2$, and -1 at $\bf R^3$ and $\bf R^4$. Meanwhile, a pair of newly emerging degeneracies have the monopole charge +1 and -1 at $\bf R^2$ and $\bf R^1$ points, respectively. The topological analysis is further supported by the Brillouin zone evolution of the first Chern number, defined analogously to the charge as

$$C(P) = \frac{1}{2\pi} \int_{P} \mathbf{\Omega}(\mathbf{k}) \cdot \mathbf{n} \, dP, \tag{7}$$

where P is a two-dimensional slice of the Brillouin zone and \mathbf{n} is its normal. By defining the plane P as the k_x - k_y plane at a given k_z with $\mathbf{n} = (0, 0, 1)$, we compute the evolution of $C(k_z)$ as a function of k_z , presenting the results in Fig. S5 of the Supplemental Material [56]. Without DMI, the Chern number changes by 2 when P passes through the degenerate crossing points, while in the presence of DMI it changes by 1 when P passes through every nondegenerate crossing point. This analysis underlines the main finding of our paper—the emergence of two doubly degenerate type-I Weyl points [58] in the magnonic structure of Cu_2OSeO_3 , located at \mathbf{R} and $\mathbf{\Gamma}$ without DMI, which further split into four Weyl points overall when the symmetry of the system is reduced by including the DMI into consideration, while the latter additionally drives an emergence of a new pair of Weyl points near \mathbf{R} .

C. Surface states

As the emergence of the Weyl points in the magnonic band structure of a three-dimensional crystal is expected to give rise to the surface states of a thin film, here, we analyze the magnon band structure of a 75-layer-thick two-dimensional slab of Cu_2OSeO_3 cut along the [001] axis, presenting the results in Fig. 3. The spin-wave dispersion is shown along the path which includes the projections of the Weyl points onto the (001) plane, which are further indicated with small red and blue circles in the figure, according to their topological charge. In the magnon band structure, the states are marked with their weight at the surface of the slab (see Supplemental Material

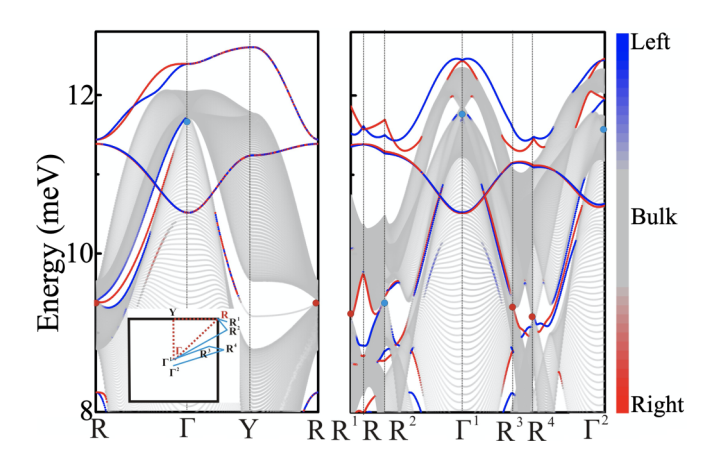


FIG. 3. The surface magnon band structure of the 75-layer-thick slab of $Cu_2OSeO_3(001)$ along the paths indicated in the inset shown on the left without the DMI, and on the right including the DMI. The special points Γ , R, Γ^1 , R^1 , Γ^2 , R^2 , R^3 , and R^4 are the projections of the Weyl points onto the (001) plane, which are indicated with red (positive charge) and blue (negative charge) solid circles. The color scale represents the weight of the magnonic wave function along the slab.

[56] for more details). The left plot in Fig. 3 corresponds to the situation without the DMI, with projections of the Weyl points positioned at high-symmetry points in the two-dimensional Brillouin zone. We observe that in this case the Weyl points of opposite chirality are connected by the magnon "arc" surface states, which is in accord with our topological analysis from above. Upon including the effect of the DMI, the Weyl points split, and their projections move to the Γ^1 , R^3 , Γ^2 , and R^4 points. Meanwhile, one pair of Weyl points appears at R^1 and R^2 points. Again, this is consistent with the previous analysis of the topological charges: While the points of the same charge are not connected by the surface states, the points of opposite chirality are. An additional analysis of the surface magnon arcs and surface band structure is given in the Supplemental Material [56].

D. Thermal Hall conductivity

The topological thermal Hall effect of magnons is the generation of a transverse thermal Hall voltage under an applied longitudinal temperature gradient due to the presence of the DMI [59,60].

The energy-dependent contribution to the ijth Cartesian component of the thermal Hall conductivity tensor \hat{k} can be calculated from the corresponding component of the Berry curvature tensor as

$$\kappa^{ij}(\epsilon) = -\frac{k_{\rm B}^2 T}{(2\pi)^3 \hbar} \sum_n \int_{\rm BZ} \delta(\epsilon_{n\mathbf{k}} - \epsilon) C_2(f_n^{\rm B}) \Omega_n^{ij}(\mathbf{k}) d\mathbf{k}, \quad (8)$$

where n enumerates the magnon bands, $f_n^{\rm B}$ is the Bose-Einstein distribution function, which can be expressed as $f_n^{\rm B} = (e^{\epsilon_{n{\bf k}}/k_{\rm B}T}-1)^{-1}$, and C_2 is given by

$$C_2(x) = (1+x)\left(\ln\frac{1+x}{x}\right)^2 - \ln^2 x - 2\operatorname{Li}_2(-x),$$
 (9)

with Li₂ denoting the dilogarithm function. The thermal Hall conductivity tensor of the system is then defined as

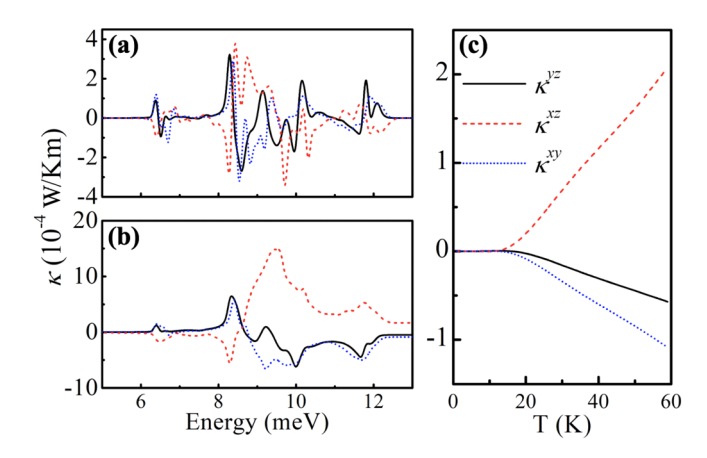


FIG. 4. Components of the thermal Hall conductivity tensor in Cu_2OSeO_3 . (a) Energy-dependent and (b) cumulative thermal Hall conductivity computed at 60 K. (c) The temperature dependence of the thermal Hall conductivity.

 $\kappa^{ij}=\lim_{\mu\to\infty}\kappa^{ij}_{\mu}$, where $\kappa^{ij}_{\mu}=\int_0^\mu\kappa^{ij}(\epsilon)d\varepsilon$ is the cumulative thermal Hall conductivity.

From experiment we know that the Curie temperature of Cu_2OSeO_3 is around 60 K [42,45]. The computed energy dependence and the cumulative components of the thermal Hall conductivity, calculated according to equations above at 60 K, are shown in Figs. 4(a) and 4(b). In these plots we observe that in the energy region between 8 and 10 meV there is a sig-

nificant enhancement, especially in the κ^{xz} component of the thermal Hall conductivity. This enhancement can be attributed to the distribution of the Berry curvature around the Weyl points in that energy region, which correspondingly gives rise to the fingerprint of the Weyl points in the energy distribution of the thermal Hall effect. Since the Weyl-point enhancement is most prominent for the κ^{xz} component, the overall value of the thermal Hall conductivity for this component is by far dominant over the other two components at 60 K [see Fig. 4(c), where the thermal Hall conductivity as a function of temperature is shown]. As magnons obey the Bose-Einstein distribution, and the low-lying states are thus responsible for the thermal Hall effect at low temperatures, the characteristic zero plateau in κ observed in Fig. 4(c) is a consequence of the vanishing contribution by the "topologically trivial" low-lying bands which are basically not affected by the DMI [Fig. 1(d)]. Respectively, the thermal Hall effect "lifts off" once the region of Weyl points is reached by the distribution of magnons. The overall magnitude of the thermal Hall effect that we predict in the region of higher temperatures can reach as much as 2×10^{-4} W/K m, which is large enough to be observed in experiments [59,60].

E. Effect of the DMI on Weyl points and thermal Hall effect

Given the low structural symmetry of Cu₂OSeO₃, it seems reasonable to explore the influence of the direction and

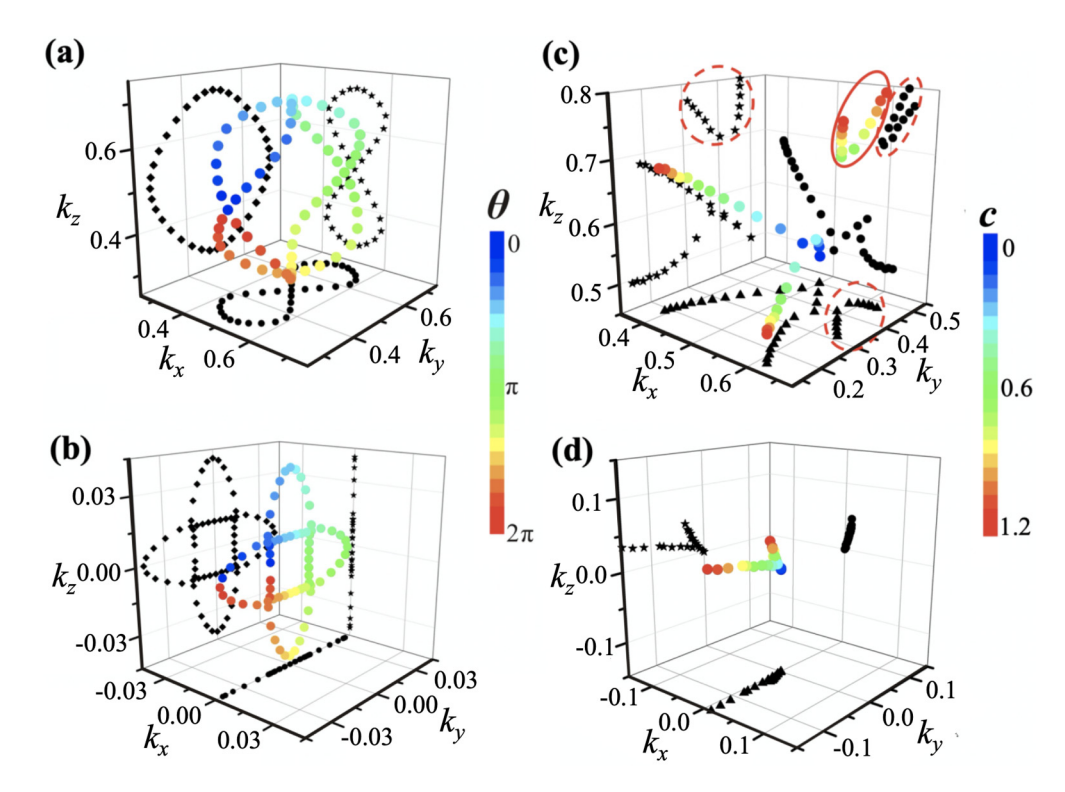


FIG. 5. The effect of the nearest-neighbor Dzyaloshinskii-Moriya coupling on the positions of the Weyl points. (a), (b) The DMI vector is rotated about the x axis with the initial direction along [010], and the evolution of the corresponding Weyl points with angle θ near (a) \mathbf{R} and (b) $\mathbf{\Gamma}$ points is shown. The projection of each Weyl point onto the k_x - k_y , k_x - k_z , and k_y - k_z planes is shown with black symbols in the corresponding planes. (c), (d) The evolution of the Weyl points near (c) \mathbf{R} and (d) $\mathbf{\Gamma}$ as a function of the DMI strength, with the DMI vector following D = c(-0.491, 2.0, -1.41) meV, where the coefficient c represented by the color scale is chosen from 0 to 1.2. The red circle marks a new pair of Weyl points as c increases, and the projections are circled by red dotted circles.

strength of the DMI vector on the position of the Weyl points in the Brillouin zone. While we envisage that the tuning of the DMI parameters can be realized, e.g., by pressure, strain, electric field [61–64], or doping with defects, knowing the correlation between the Weyl point geometry and the DMI provides a unique tool for accessing the details of the DMI in a given sample, which are challenging to extract with other techniques based, e.g., on measuring the properties of domain walls [65,66].

To estimate the influence of the DMI on the Weyl points, we first keep the direction of the DMI along the fitted DMI direction, while scaling its magnitude following D = c(-0.491, 2.0, -1.41) meV [c is the coefficient represented by the color scale in Figs. 5(c) and 5(d)]. The evolution of the Weyl points around \mathbf{R} and $\mathbf{\Gamma}$ upon increasing the DMI is shown in Figs. 5(c) and 5(d) separately. Notably, upon starting from a degenerate case at zero DMI, the splitting between the two Weyl points is clearly driven by lowering of symmetry upon including the nonvanishing DMI. When the value of the coefficient c continues to increase and eventually approaches 0.5, a new pair of Weyl points appears near the \mathbf{R} point, which is indicated by the red circle.

Further, after fixing the magnitude of the DMI to the value of 1 meV, we rotate the direction of the nearest-neighbor DMI vector, as specified by angle θ , about the x axis, and track the position of two Weyl points around Γ and R in Figs. 5(b) and 5(a), respectively. The results indicate that the Weyl points rotate around the R and Γ points along specific paths when following the rotation of the DMI vector. The corresponding trajectories, while having a relatively complex shape in the three-dimensional Brillouin zone, clearly possess a high degree of symmetry, as apparent from the projections of the trajectories onto the high-symmetry planes [see, e.g., Figs. 5(a) and 5(b)]. We show further data on the correlation between the DMI and the Weyl point behavior in the Supplemental Material [56].

In addition to systematically investigating the influence of DMI on the Weyl points, we also address the relationship between the thermal Hall effect and the DMI. To do this, under the premise of ensuring the agreement with the experimental magnon dispersion, the magnon dispersion and thermal Hall conductivity are calculated for a different choice of the DMI vector, which gives rise to a different number of Weyl points. As we show in the Supplemental Material [56], four Weyl points which are observed in the first Brillouin zone as a result of this specific choice of the DMI result in a magnitude of the thermal Hall conductivity which is smaller by about one order of magnitude than the one discussed in the paper. These results suggest that the thermal Hall conductivity in this compound is directly related to the position and number of Weyl points modulated in turn by the microscopics of the DMI.

III. DISCUSSION

In our work, based on the spin-wave theory and experiment, we arrived at several important findings concerning the spin-wave properties of ferrimagnetic Cu₂OSeO₃. First, we were able to attribute the origin of the experimentally observed magnon band gap in the spin-wave spectrum at the **R** point to the effect of the DMI, which was chosen so as to

provide the best fit to the high-resolution neutron scattering data. Second, after systematically addressing the topological properties of Cu₂OSeO₃, we uncovered the emergence of the doubly degenerate Weyl nodes with a topological charge ± 2 at the high-symmetry points even without the effect of the DMI. We further predicted that not only does each Weyl point split into two, but also one additional pair of Weyl points appears near the **R** point as the symmetry of the system is reduced when bringing the DMI into play. The proximity of several bands makes it difficult to resolve the bands forming the Weyl crossing point from the other two modes, yet from the overall agreement of the calculations with the experimental measurements one can conclude that our previously proposed fitting parameters must be valid within the present accuracy of the experiment. Importantly, we find that the position and number of the Weyl points can be controlled by changing the details of the atomic arrangement in the compound. We further predict that the emergence of the Weyl points in the system goes hand in hand with the formation of topological magnonic surface states, which can be observed, for instance, at the (001) surface of Cu₂OSeO₃.

Our findings open a quest for the experimental observation of the Weyl points in this material, and exploring the influence of such points in the spin-wave spectrum on various properties of more complex magnetic phases in Cu₂OSeO₃, for example, its skyrmion phase. While we discover that Weyl points play a crucial role in shaping the magnitude and temperature dependence of the thermal Hall effect in its ferrimagnetic phase, we expect that the same holds true also for skyrmions in Cu₂OSeO₃. The observation of the exact position of the Weyl points as well as following their dynamics upon structural reconstructions in Cu₂OSeO₃ can further provide a unique tool for accessing the microscopics of the DMI in this complex compound, which can be of paramount importance for understanding and shaping the chiral dynamics and properties of Cu₂OSeO₃. The latter finding also suggests that in special materials of Cu₂OSeO₃ type, one can expect that the topologies in the space of magnons and in the real space of skyrmions can be closely intertwined.

ACKNOWLEDGMENTS

We acknowledge fruitful discussions with Flaviano José dos Santos, Sergii Grytsiuk, Matthias Redies, Lizhi Zhang, and Wanxiang Feng. This project was supported by the China Scholarship Council (CSC) (Grant No. [2016]3100) and by the German Research Foundation (DFG) within the project C03 of the Collaborative Research Center SFB 1143 at the TU Dresden (project-id 247310070), the Würzburg-Dresden Cluster of Excellence on Complexity and Topology in Quantum Matter - ct.qmat (EXC 2147, project-id 39085490), the individual research Grants No. IN 209/4-1 and No. MO 1731/5-1, and the priority programme SPP 2137 "Skyrmionics" (Projects No. IN 209/7-1 and No. MO 1731/7-1). This work has been also supported by the DFG through the Collaborative Research Centers SFB 1238 and SFB/TRR 173. We gratefully acknowledge computing time on the supercomputers of Jülich Supercomputing Center, and at the JARA-HPC cluster of RWTH Aachen.

- [1] B. A. Bernevig, *Topological Insulators and Topological Super-conductors* (Princeton University Press, Princeton, NJ, 2013).
- [2] *Topological Insulators*, edited by F. Ortmann, S. Roche, and S. O. Valenzuela (Wiley-VCH, Weinheim, 2015).
- [3] A. Bansil, H. Lin, and T. Das, Rev. Mod. Phys. 88, 021004 (2016).
- [4] N. P. Armitage, E. J. Mele, and A. Vishwanath, Rev. Mod. Phys. 90, 015001 (2018).
- [5] Topology in Magnetism, edited by J. Zang, V. Cros, and A. Hoffmann (Springer, Berlin, 2018).
- [6] S.-Y. Xu, I. Belopolski, N. Alidoust, M. Neupane, G. Bian, C. Zhang, R. Sankar, G. Chang, Z. Yuan, C.-C. Lee *et al.*, Science 349, 613 (2015).
- [7] B. Q. Lv, H. M. Weng, B. B. Fu, X. P. Wang, H. Miao, J. Ma, P. Richard, X. C. Huang, L. X. Zhao, G. F. Chen, Z. Fang, X. Dai, T. Qian, and H. Ding, Phys. Rev. X 5, 031013 (2015).
- [8] L. Lu, Z. Wang, D. Ye, L. Ran, L. Fu, J. D. Joannopoulos, and M. Soljačić, Science 349, 622 (2015).
- [9] L. Lu, J. D. Joannopoulos, and M. Soljačić, Nat. Photonics 8, 821 (2014).
- [10] F. Li, X. Huang, J. Lu, J. Ma, and Z. Liu, Nat. Phys. 14, 30 (2018).
- [11] R. Chisnell, J. S. Helton, D. E. Freedman, D. K. Singh, R. I. Bewley, D. G. Nocera, and Y. S. Lee, Phys. Rev. Lett. 115, 147201 (2015).
- [12] W. Yao, C. Li, L. Wang, S. Xue, Y. Dan, K. Iida, K. Kamazawa, K. Li, C. Fang, and Y. Li, Nat. Phys. 14, 1011 (2018).
- [13] S. Bao, J. Wang, W. Wang, Z. Cai, S. Li, Z. Ma, D. Wang, K. Ran, Z.-Y. Dong, D. L. Abernathy *et al.*, Nat. Commun. 9, 2591 (2018).
- [14] L. Zhang, J. Ren, J.-S. Wang, and B. Li, Phys. Rev. B 87, 144101 (2013).
- [15] S. A. Owerre, J. Phys.: Condens. Matter 28, 386001 (2016).
- [16] K. Nakata, S. K. Kim, J. Klinovaja, and D. Loss, Phys. Rev. B 96, 224414 (2017).
- [17] B. Li and A. A. Kovalev, Phys. Rev. B 97, 174413 (2018).
- [18] R. Schaffer, E. K.-H. Lee, Y.-M. Lu, and Y. B. Kim, Phys. Rev. Lett. **114**, 116803 (2015).
- [19] F.-Y. Li, Y.-D. Li, Y. B. Kim, L. Balents, Y. Yu, and G. Chen, Nat. Commun. 7, 12691 (2016).
- [20] A. Mook, J. Henk, and I. Mertig, Phys. Rev. Lett. 117, 157204 (2016).
- [21] K. Li, C. Li, J. Hu, Y. Li, and C. Fang, Phys. Rev. Lett. 119, 247202 (2017).
- [22] N. Okuma, Phys. Rev. Lett. 119, 107205 (2017).
- [23] F.-Y. Li, Y.-D. Li, Y. Yu, A. Paramekanti, and G. Chen, Phys. Rev. B 95, 085132 (2017).
- [24] F.-Y. Li and G. Chen, Phys. Rev. B 98, 045109 (2018).
- [25] S.-K. Jian and W. Nie, Phys. Rev. B 97, 115162 (2018).
- [26] S. A. Owerre, Sci. Rep. 8, 10098 (2018).
- [27] L. Šmejkal, T. Jungwirth, and J. Sinova, Phys. Status Solidi RRL 11, 170044 (2017).
- [28] L. Šmejkal, Y. Mokrousov, B. Yan, and A. H. MacDonald, Nat. Phys. 14, 242 (2018).
- [29] A. Rückriegel, A. Brataas, and R. A. Duine, Phys. Rev. B **97**, 081106(R) (2018).
- [30] X. S. Wang, H. W. Zhang, and X. R. Wang, Phys. Rev. Applied 9, 024029 (2018).
- [31] I. Dzyaloshinsky, J. Phys. Chem. Solids 4, 241 (1958).

- [32] T. Moriya, Phys. Rev. 120, 91 (1960).
- [33] S. Seki, X. Yu, S. Ishiwata, and Y. Tokura, Science 336, 198 (2012).
- [34] S. Seki, J.-H. Kim, D. S. Inosov, R. Georgii, B. Keimer, S. Ishiwata, and Y. Tokura, Phys. Rev. B 85, 220406(R) (2012).
- [35] M. C. Langner, S. Roy, S. K. Mishra, J. C. T. Lee, X. W. Shi, M. A. Hossain, Y.-D. Chuang, S. Seki, Y. Tokura, S. D. Kevan, and R. W. Schoenlein, Phys. Rev. Lett. 112, 167202 (2014).
- [36] M. C. Langner, S. Roy, S. W. Huang, J. D. Koralek, Y.-D. Chuang, G. L. Dakovski, J. J. Turner, J. S. Robinson, R. N. Coffee, M. P. Minitti, S. Seki, Y. Tokura, and R. W. Schoenlein, Phys. Rev. Lett. 119, 107204 (2017).
- [37] J. Müller, J. Rajeswari, P. Huang, Y. Murooka, H. M. Rønnow, F. Carbone, and A. Rosch, Phys. Rev. Lett. 119, 137201 (2017).
- [38] H. Effenberger and F. Pertlik, Monatsh. Chem. 117, 887 (1986).
- [39] P. Y. Portnichenko, J. Romhányi, Y. A. Onykiienko, A. Henschel, M. Schmidt, A. S. Cameron, M. A. Surmach, J. A. Lim, J. T. Park, A. Schneidewind *et al.*, Nat. Commun. 7, 10725 (2016).
- [40] J. H. Yang, Z. L. Li, X. Z. Lu, M.-H. Whangbo, S.-H. Wei, X. G. Gong, and H. J. Xiang, Phys. Rev. Lett. 109, 107203 (2012).
- [41] J. Romhányi, J. van den Brink, and I. Rousochatzakis, Phys. Rev. B 90, 140404(R) (2014).
- [42] O. Janson, I. Rousochatzakis, A. A. Tsirlin, M. Belesi, A. A. Leonov, U. K. Rößler, J. van den Brink, and H. Rosner, Nat. Commun. 5, 5376 (2014).
- [43] V. A. Chizhikov and V. E. Dmitrienko, J. Magn. Magn. Mater. 382, 142 (2015).
- [44] M. Ozerov, J. Romhányi, M. Belesi, H. Berger, J.-P. Ansermet, J. van den Brink, J. Wosnitza, S. A. Zvyagin, and I. Rousochatzakis, Phys. Rev. Lett. 113, 157205 (2014).
- [45] G. S. Tucker, J. S. White, J. Romhányi, D. Szaller, I. Kézsmárki, B. Roessli, U. Stuhr, A. Magrez, F. Groitl, P. Babkevich, P. Huang, I. Zivkovic, and H. M. Ronnow, Phys. Rev. B 93, 054401 (2016).
- [46] J.-W. G. Bos, C. V. Colin, and T. T. M. Palstra, Phys. Rev. B 78, 094416 (2008).
- [47] M. Belesi, I. Rousochatzakis, H. C. Wu, H. Berger, I. V. Shvets, F. Mila, and J. P. Ansermet, Phys. Rev. B 82, 094422 (2010).
- [48] K. H. Miller, X. S. Xu, H. Berger, E. S. Knowles, D. J. Arenas, M. W. Meisel, and D. B. Tanner, Phys. Rev. B 82, 144107 (2010).
- [49] S. Toth and B. Lake, J. Phys.: Condens. Matter 27, 166002 (2015).
- [50] F. J. dos Santos, M. dos Santos Dias, F. S. M. Guimarães, J. Bouaziz, and S. Lounis, Phys. Rev. B 97, 024431 (2018).
- [51] S. A. Owerre, Phys. Rev. B 97, 094412 (2018).
- [52] T. Holstein and H. Primakoff, Phys. Rev. 58, 1098 (1940).
- [53] A. Schneidewind and P. Čermák, J. Large-Scale Res. Facilities 1, A12 (2015).
- [54] R. A. Ewings, J. R. Stewart, T. G. Perring, R. I. Bewley, M. D. Le, D. Raspino, D. E. Pooley, G. Škoro, S. P. Waller, D. Zacek, C. A. Smith, and R. C. Riehl-Shaw, Rev. Sci. Instrum. 90, 035110 (2019).
- [55] D. Inosov *et al.*, Topological magnons in Cu₂OSeO₃, STFC ISIS Neutron and Muon Source, doi:10.5286/ISIS.E.RB1910425 (2019).

- [56] See Supplemental Material at http://link.aps.org/supplemental/ 10.1103/PhysRevResearch.2.013063 for technical details of the calculations.
- [57] S. Shivam, R. Coldea, R. Moessner, and P. McClarty, arXiv:1712.08535.
- [58] A. A. Soluyanov, D. Gresch, Z. Wang, Q.-S. Wu, M. Troyer, X. Dai, and B. A. Bernevig, Nature (London) 527, 495 (2015).
- [59] Y. Onose, T. Ideue, H. Katsura, Y. Shiomi, N. Nagaosa, and Y. Tokura, Science 329, 297 (2010).
- [60] M. Hirschberger, R. Chisnell, Y. S. Lee, and N. P. Ong, Phys. Rev. Lett. 115, 106603 (2015).
- [61] A. W. J. Wells, P. M. Shepley, C. H. Marrows, and T. A. Moore, Phys. Rev. B 95, 054428 (2017).

- [62] Y. Nii, T. Nakajima, A. Kikkawa, Y. Yamasaki, K. Ohishi, J. Suzuki, Y. Taguchi, T. Arima, Y. Tokura, and Y. Iwasa, Nat. Commun. 6, 8539 (2015).
- [63] T. Srivastava, M. Schott, R. Juge, V. Krizakova, M. Belmeguenai, Y. Roussigné, A. Bernand-Mantel, L. Ranno, S. Pizzini, S.-M. Chérif *et al.*, Nano Lett. 18, 4871 (2018).
- [64] T. Koyama, Y. Nakatani, J. Ieda, and D. Chiba, Sci. Adv. 4, eaav0265 (2018).
- [65] K.-S. Ryu, L. Thomas, S.-H. Yang, and S. Parkin, Nat. Nanotechnol. 8, 527 (2013).
- [66] S. Emori, U. Bauer, S.-M. Ahn, E. Martinez, and G. S. Beach, Nat. Mater. 12, 611 (2013).